Nonlinear Model Predictive Control for Integrated Energy-Efficient Torque-Vectoring and Anti-Roll Moment Distribution

Matteo Dalboni, Davide Tavernini [ORCID], Umberto Montanaro [ORCID], Alessandro Soldati [ORCID], *Member, IEEE*, Carlo Concari [ORCID], *Member, IEEE*, Miguel Dhaens, and Aldo Sorniotti [ORCID], *Member, IEEE*

Abstract—**This study applies nonlinear model predictive control (NMPC) to the torque-vectoring (TV) and front-to-total anti-roll moment distribution control of a four-wheel-drive electric vehicle with in-wheel-motors, a brake-by-wire system, and active suspension actuators. The NMPC cost function formulation is based on energy efficiency criteria, and strives to minimize the power losses caused by the longitudinal and lateral tire slips, friction brakes, and electric powertrains, while enhancing the vehicle cornering response in steady-state and transient conditions. The controller is assessed through simulations using an experimentally validated high-fidelity vehicle model, along ramp steer and multiple step steer maneuvers, including and excluding the direct yaw moment and active anti-roll moment distribution actuations. The results show: 1) the substantial enhancement of energy saving and vehicle stabilization performance brought by the integration of the active suspension contribution and TV; 2) the significance of the power loss terms of the NMPC formulation on the results; and 3) the effectiveness of the NMPC with respect to the benchmarking feedback and rule based controllers.**

Index Terms—**Anti-roll moment distribution control, nonlinear model predictive control (NMPC), power loss, torque-vectoring (TV).**

I. INTRODUCTION

TORQUE-VECTORING (TV) control, i.e., the modulation of the wheel torque distribution among the four vehicle

corners, including generation of a direct yaw moment, has gained interest in recent years for passenger cars, with increasingly frequent experimental demonstrations on electric vehicles with multiple powertrains [1]. TV allows: 1) shaping the understeer characteristic, i.e., the level of lateral acceleration for given steering angle and vehicle speed [1]; 2) enhancing yaw and sideslip damping in extreme transients [1]; and 3) reducing energy consumption during straight line and cornering operation [2]–[6]. In this respect, the most recent TV implementations include consideration of the power losses related to longitudinal and lateral tire slip as well as electric powertrains [6].

In modern passenger cars, another typology of chassis actuation is represented by active suspension control. Active suspension systems are normally used for: 1) active body control, i.e., for reducing the motion of the sprung mass induced by the longitudinal and lateral accelerations during traction/braking and cornering; 2) ride comfort control, to limit the vehicle body heave, pitch and roll accelerations provoked by road irregularities; and 3) road holding control, expressed through the reduction of the variation of the normal tire load on irregular surfaces. However, active suspension systems also allow the control of the anti-roll moment distribution between the front and rear axles [7]–[10]. In cornering, the increase of the anti-roll moment, and thus of the lateral load transfer within the axle, tends to decrease the lateral axle force for a given slip angle [10]. Hence, the increase of the anti-roll moment on the front axle and/or a decrease on the rear axle brings increased understeer; vice versa, increased anti-roll moment distribution toward the rear axle reduces understeer. This effect is particularly evident at medium-to-high lateral accelerations, and can be used for yaw rate or sideslip angle control, similarly to TV. Given the nonlinearity of the influence of the anti-roll moment distribution on vehicle dynamics, this kind of suspension controllers is usually empirically tuned. Very recent studies [11] have proposed linearized models for considering the effect of the anti-roll moment distribution on the cornering response.

In the available active suspension research, the consideration of energy aspects is limited to the power recovery capabilities of the actuators [12]. However, during cornering, the variation of the understeer characteristic induced by front-to-total anti-roll moment distribution control has implications on the longitudinal and lateral tire slip power losses, which have not been explored yet. Moreover, integrated TV and active suspension control

TABLE I
MAIN VEHICLE PARAMETERS

Description	Symbol	Value	Unit
Front semi-wheelbase	a_F	1.47	m
Rear semi-wheelbase	a_R	1.46	m
Front track width	b_F	1.66	m
Rear track width	b_R	1.66	m
Center of gravity height	h_{CG}	0.63	m
Wheel radius	R	0.37	m
Total mass	m	2843	kg
Roll mass moment of inertia	J_x	550	kg m^2
Yaw mass moment of inertia	J_z	5291	kg m^2

Fig. 1. (a) Top view and (b) rear view of the vehicle with indication of the main variables and parameters.

could enhance the cornering response and energy efficiency with respect to the independent control of the actuators. The study in [13] is one of the very few contributions in this area, and deals with the concurrent actuation of active aerodynamics, active rear steering, TV, and hydraulically interconnected suspensions. However, the controllers are coexistent rather than integrated, and the suspension system is passive–even if it is based on an advanced hydraulic layout–rather than active. The implementation in [14] includes two feedback controllers–one for the reference direct yaw moment and a second one for the reference anti-roll moment distribution–using the same reference yaw rate. In [15], a simplified model, assuming linear relationship between slip angle and lateral tire force, is used to calculate the anti-roll moments generating the reference yaw moment, and, if this is not feasible through the active anti-roll bars, the friction brakes are actuated. In the integrated controller in [16], the control effectiveness matrix empirically imposes the difference between the front and rear anti-roll moments to be directly proportional to the one between the front and rear slip angles.
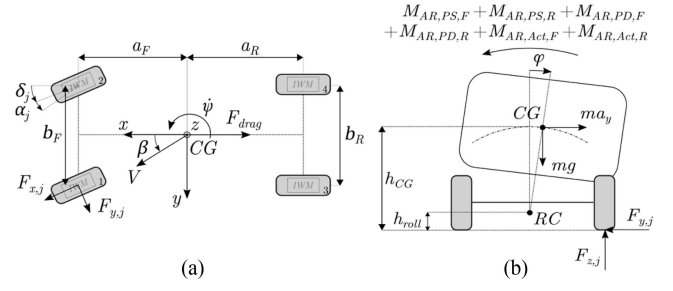
In conclusion, to the best of our knowledge, the literature has a gap on the integrated and optimal model based control of the wheel torque and anti-roll moment distributions. A fortiori, there are not integrated TV and active suspension controllers with consideration of vehicle energy consumption aspects. This study targets the identified gap with the following contributions.

1) A novel nonlinear model predictive control (NMPC) implementation for integrated TV and anti-roll moment distribution control, including consideration of the power losses associated with the electric powertrains, tires, and friction brakes.

2) The performance comparison of the proposed NMPC with benchmarking feedback controllers based on proportional integral (PI) technology.

The case study vehicle, considered in the European project EVC1000 [17], see its main parameters in Table I, is simulated with a high-fidelity and experimentally validated simulation model, and is equipped with four in-wheel motors (IWMs), a brake-by-wire system with independent control of the clamping force of each brake caliper, and active suspension actuators.

The rest of the article is organized as follows. Section II deals with the internal model formulation. Section III describes the nonlinear optimal control problem. Section IV discusses the simulation results. Finally, Section V summarizes the main conclusions.

II. INTERNAL MODEL FORMULATION

The adopted internal model, i.e., the model used by the NMPC for predicting the system response along the prediction horizon [18], has 8 degrees of freedom, described by (1) and (3)–(6) (see Fig. 1 for the nomenclature and sign conventions), which are in explicit form with respect to the time derivatives of the states.

1) Longitudinal force balance

$$\dot{V} = \frac{1}{m} \left\{ \cos(\beta) \left\{ \sum_{j=1}^{4} [F_{x,j}\cos(\delta_j) - F_{y,j}\sin(\delta_j)] - F_{drag} \right\} \right.$$
$$\left. + \sin(\beta) \sum_{j=1}^{4} [F_{x,j}\sin(\delta_j) + F_{y,j}\cos(\delta_j)] \right\} \quad (1)$$

where m is the vehicle mass; V is the magnitude of the speed of the center of mass; β is the sideslip angle; $\dot{\psi}$ is the yaw rate; $F_{x,j}$ and $F_{y,j}$ are the longitudinal and lateral tire forces of the j-th wheel, expressed in the wheel reference frame; δ_j is the steering angle of the j-th wheel, comprehensive of the respective toe angle contribution; and F_{drag} is the aerodynamic drag force, which is given by

$$F_{drag} = 0.5\rho_{air}AC_d[V\cos(\beta)]^2 \quad (2)$$

where ρ_{air} is the air density; A is the vehicle frontal cross-section; and C_d is the aerodynamic drag coefficient.

2) Lateral force balance

$$\dot{\beta} = \frac{1}{mV} \left\{ \cos(\beta) \sum_{j=1}^{4} [F_{x,j}\sin(\delta_j) + F_{y,j}\cos(\delta_j)] \right.$$
$$\left. - \sin(\beta) \left\{ \sum_{j=1}^{4} [F_{x,j}\cos(\delta_j) - F_{y,j}\cos(\delta_j)] - F_{drag} \right\} \right\} - \dot{\psi} \quad (3)$$

under the common assumption of neglecting the lateral displacement of the center of gravity caused by the roll motion, as this aspect has only a very marginal effect on the resulting cornering response, and the approximation allows significant reduction of the computational load.

3) Yaw moment balance

$$\ddot{\psi} = \frac{1}{J_z} \left\{ \sum_{j=1}^{2} a_F \left[F_{x,j} \sin(\delta_j) + F_{y,j} \cos(\delta_j) \right] \right.$$

$$- \sum_{j=3}^{4} a_R \left[F_{x,j} \sin(\delta_j) + F_{y,j} \cos(\delta_j) \right]$$

$$- \frac{b_F}{2} \left[F_{x,1} \cos(\delta_1) - F_{y,1} \sin(\delta_1) \right]$$

$$+ \frac{b_F}{2} \left[F_{x,2} \cos(\delta_2) - F_{y,2} \sin(\delta_2) \right]$$

$$- \frac{b_R}{2} \left[F_{x,3} \cos(\delta_3) - F_{y,3} \sin(\delta_3) \right]$$

$$\left. + \frac{b_R}{2} \left[F_{x,4} \cos(\delta_4) - F_{y,4} \sin(\delta_4) \right] \right\} \quad (4)$$

where J_z is the yaw mass moment of inertia of the vehicle; a_F and a_R are the front and rear semiwheelbases; and b_F and b_R are the front and rear track widths.

4) Roll moment balance

$$\ddot{\varphi} = \frac{1}{J_x} \left\{ m a_{y,ext} [h_{CG} - h_{roll}] \cos(\varphi) \right.$$

$$+ mg[h_{CG} - h_{roll}] \sin(\varphi)$$

$$- M_{AR,PS,F} - M_{AR,PS,R} - M_{AR,PD,F}$$

$$\left. - M_{AR,PD,R} - M_{AR,Act,F} - M_{AR,Act,R} \right\} \quad (5)$$

where φ is the roll angle; J_x is the roll mass moment of inertia; $a_{y,ext}$ is the lateral acceleration, which is the one measured by the vehicle's inertial measurement unit, and is kept constant along the prediction horizon; h_{CG} is the center of gravity height from the ground in static conditions; h_{roll} is the roll axis height from the ground at the longitudinal position of the center of gravity; g is the gravitational acceleration; $M_{AR,PS,}$ and $M_{AR,PS,}$ are the front and rear anti-roll moment contributions of the passive springs and anti-roll bars; $M_{AR,PD,F}$ and $M_{AR,PD,R}$ are the front and rear anti-roll moment contributions of the passive dampers; and $M_{AR,Act,F}$ and $M_{AR,Act,R}$ are the front and rear anti-roll moment contributions generated by the active suspension actuators. The approximation of considering $a_{y,ext}$ in (5), instead of the predicted acceleration profile, increases the computational efficiency without compromising the results, as the scope of the proposed nonlinear optimal control problem is to optimize the vertical tire load distribution to allow the vehicle to achieve desirable cornering response and minimize power consumption, rather than controlling roll angle.

5) j-th wheel moment balance

$$\dot{\Omega}_j = \frac{1}{J_{w,j}} \left[T_j - F_{x,j} R_j - M_{y,j} \right] \quad (6)$$

where Ω_j is the rotational speed of the j-th wheel; $J_{w,j}$ is the wheel mass moment of inertia; R_j is the wheel radius; $M_{y,j}$ is the rolling resistance moment; and T_j is the wheel torque, sum of the IWM torque, $T_{el,j}$, and friction braking torque, $T_{bk,j}$, the

latter being relevant only for $T_j < 0$:

$$T_j = T_{el,j} + T_{bk,j}. \quad (7)$$

$M_{y,j}$ is given by

$$M_{y,j} = F_{z,j} \left\{ k_0 + k_1 [R_{e,j} \Omega_j]^2 \right\} R_j \quad (8)$$

in which k_0 and k_1 are constant coefficients; $F_{z,j}$ is the vertical tire load; and $R_{e,j}$ is the effective rolling radius.

To achieve an integral yaw rate tracking contribution, the integral $e_{int,\psi}$ of the yaw rate error is formulated as an augmented system state

$$\dot{e}_{int,\psi} = \dot{\psi} - \dot{\psi}_{ref} \quad (9)$$

where $\dot{\psi}_{ref}$ is the reference yaw rate. Within the internal model, for each vehicle corner the brake blending formulation prioritizes regenerative braking over friction braking, through the following smooth saturation formulation, which approximates $T_{el,j} = \max(T_j, T_{el,min,j})$ and is suitable for the numerical implementation of the NMPC algorithm

$$T_{el,j} = \frac{T_j - T_{el,min,j}}{1 + e^{-w_{ss}[T_j - T_{el,min,j}]}} + T_{el,min,j} \quad (10)$$

where $T_{el,min,j} \le 0$ is the minimum electric motor torque; and w_{ss} is a positive coefficient that defines the desired degree of smoothness. The friction brake torque, $T_{bk,j}$, is defined by $T_{bk,j} = T_j - T_{el,j}$.

In a first approximation, the passive anti-roll moment contributions can be calculated as linear functions of the roll angle and roll rate

$$M_{AR,PS,i} = k_{s,i} \varphi$$

$$M_{AR,PD,i} = k_{d,i} \dot{\varphi} \quad (11)$$

where the subscript $i = F, R$ indicates the front and rear axles; and $k_{s,i}$ and $k_{d,i}$ are the suspension roll stiffness and damping coefficient. The active anti-roll moment contributions are expressed as follows:

$$M_{AR,Act,F} = f M_{AR,Act,tot}$$

$$M_{AR,Act,R} = [1 - f] M_{AR,Act,tot} \quad (12)$$

where $f \in [0, 1]$ is the front-to-total anti-roll moment distribution factor; and $M_{AR,Act,tot}$ is the total active anti-roll moment, given by a linear function of the lateral acceleration

$$M_{AR,Act,tot} = w_r m a_{y,ext} [h_{CG} - h_{roll}] \quad (13)$$

where w_r is a scaling coefficient that is tuned according to the desired roll angle characteristic. The implication of (13) is that roll angle control is not involved in the NMPC optimization, as the total anti-roll moment considered in the internal model only depends on the measured lateral acceleration.

The longitudinal and lateral tire forces, $F_{x,j}$ and $F_{y,j}$, are calculated through a simplified version of the Pacejka magic formula (MF) as follows:

$$F_{x,j} = \frac{s_{x,j}}{s_j} \mu_{x0,j} F_{z,j} \quad (14)$$

$$F_{y,j} = \frac{s_{y,j}}{s_j} \, \mu_{y0,j} F_{z,j} \tag{15}$$

where $\mu_{x0,j}$ and $\mu_{y0,j}$ are given by

$$\mu_{x0,j} = D_x \, \sin \left(C_x \arctan \left(B_x s_j \right) \right) \tag{16}$$

$$\mu_{y0,j} = D_{y,j} \, \sin \left(C_y \arctan \left(B_y s_j \right) \right). \tag{17}$$

s_j is the combined theoretical slip

$$s_j = \sqrt{s_{x,j}^2 + s_{y,j}^2} \tag{18}$$

with

$$s_{x,j} = \frac{\sigma_j}{1 + \sigma_j} \tag{19}$$

$$s_{y,j} = -\frac{\tan \left(\alpha_j \right)}{1 + \sigma_j}. \tag{20}$$

The longitudinal slip ratio, σ_j, and slip angle, α_j, are defined as

$$\sigma_j = -\frac{v_{x,slip,j}}{v_{x,j}} \tag{21}$$

$$\alpha_j = \arctan \left(\frac{v_{y,slip,j}}{|v_{x,j}|} \right) \tag{22}$$

where the longitudinal and lateral slip velocities, $v_{x,slip,j}$ and $v_{y,slip,j}$, are

$$v_{x,slip,j} = v_{x,j} - \Omega_j R_{e,j} \tag{23}$$

$$v_{y,slip,j} = v_{y,j}. \tag{24}$$

The longitudinal and lateral speeds of the wheel hubs, $v_{x,j}$ and $v_{y,j}$ in (23) and (24), expressed in the wheel reference frame, are given by

$$v_{x,j} = \cos \left(\delta_j \right) \left[V \cos \left(\beta \right) + (-1)^j \frac{b_F}{2} \dot{\psi} \right]$$
$$+ \sin \left(\delta_j \right) \left[V \sin \left(\beta \right) + a_F \dot{\psi} \right] \tag{25}$$

$$v_{y,j} = -\sin \left(\delta_j \right) \left[V \cos \left(\beta \right) + (-1)^j \frac{b_F}{2} \dot{\psi} \right]$$
$$+ \cos \left(\delta_j \right) \left[V \sin \left(\beta \right) + a_F \dot{\psi} \right] \tag{26}$$

for $j = 1, 2$; whereas, for $j = 3, 4$

$$v_{x,j} = \cos \left(\delta_j \right) \left[V \cos \left(\beta \right) + (-1)^j \frac{b_R}{2} \dot{\psi} \right]$$
$$+ \sin \left(\delta_j \right) \left[V \sin \left(\beta \right) - a_R \dot{\psi} \right] \tag{27}$$

$$v_{y,j} = -\sin \left(\delta_j \right) \left[V \cos \left(\beta \right) + (-1)^j \frac{b_R}{2} \dot{\psi} \right]$$
$$+ \cos \left(\delta_j \right) \left[V \sin \left(\beta \right) - a_R \dot{\psi} \right]. \tag{28}$$

In (17), $D_{y,j}$ varies linearly with $F_{z,j}$, according to

$$D_{y,j} = d_1 \, F_{z,j} + d_2 \tag{29}$$

where d_1 and d_2 are constant coefficients. The feature in (29), not included in the previous NMPC formulations for TV control [6], is essential for active suspension control, since it allows to model the nonlinear relationship between lateral force and vertical load.

In (8), (14) and (15), the vertical tire loads are expressed as follows:

$$F_{z,j} = \frac{1}{2} \, mg \frac{a_R}{l} - \Delta F_z^x + (-1)^j \Delta F_{z,F}^y \quad j = 1, 2 \tag{30}$$

$$F_{z,j} = \frac{1}{2} \, mg \frac{a_F}{l} + \Delta F_z^x + (-1)^j \Delta F_{z,R}^y \quad j = 3, 4 \tag{31}$$

where $l = a_F + a_R$ and the longitudinal load transfer is

$$\Delta F_z^x = \frac{1}{2} \, m a_{x,ext} \frac{h_{CG}}{l}. \tag{32}$$

In (32) $a_{x,ext}$ is the longitudinal acceleration measured by the IMU, which is kept constant along the prediction horizon. The lateral load transfers are

$$\Delta F_{z,i}^y = \frac{m a_{y,ext} \left[l - a_i \right] h_{roll}}{l b_i} + \frac{M_{AR,i}}{b_i} \tag{33}$$

where $i = F, R$. In (33), $M_{AR,i}$ includes the passive and active anti-roll moment contributions. The coupling in the effect of the actuators is in the tire model in (14)–(17), as the TV control action affects s_j, while the suspension actuation affects $D_{y,j}$.

In the NMPC implementation, (1)–(33) are rearranged in the following general form:

$$\dot{x} \left(t \right) = h \left(t, x \left(t \right), u \left(t \right) \right) \tag{34}$$

where x is the state vector

$$x = \left[V, \beta, \dot{\psi}, \dot{\varphi}, \varphi, \Omega_1, \Omega_2, \Omega_3, \Omega_4, e_{int,\psi} \right]^T \tag{35}$$

t is time; and $u(t)$ is the control input vector, including the slack variables, defined in Section III.

Fig. 2 compares the tire characteristics of the case study vehicle, resulting from the reference full MF model implemented in the high-fidelity vehicle model (see Section IV), and the simplified MF formulation of the internal model of the NMPC. The internal vehicle model was validated against experimental data obtained on the baseline electric vehicle demonstrator without direct yaw moment nor active suspension control, e.g., along 40 m radius skidpad (Fig. 3) and transient steering (Fig. 4) maneuvers. The results show a good agreement between experimental data and internal model, both in steady-state and transient conditions.

## III. OPTIMAL CONTROL PROBLEM FORMULATION

A. Cost Function

The NMPC cost function, J, is expressed by the combination of multiple terms
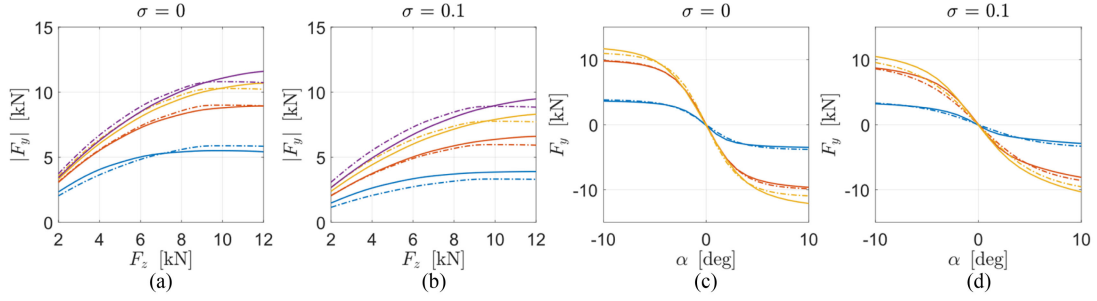
Fig. 2. Comparison of full and simplified MF models. (a) and (b): Lateral tire force as a function of vertical load for two values of the longitudinal slip ratio, 0 and 0.1. The four couples of curves correspond to slip angles equal to 2 deg (blue), 4 deg (red), 6 deg (yellow), and 8 deg (purple). (c) and (d): Lateral tire force as a function of slip angle for two values of longitudinal slip ratio, 0 and 0.1, and three vertical load levels, namely, 2 kN (blue), 7 kN (red), and 12 kN (yellow). The simplified tire model corresponds to the dash-dotted lines, while the reference full MF model corresponds to the solid lines.
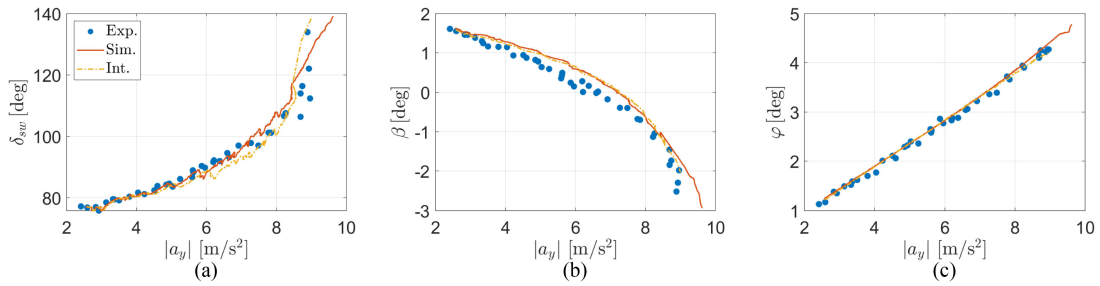
Fig. 3. Understeer, sideslip angle, and roll angle characteristics as functions of lateral acceleration (a_y) during a 40 m radius skidpad maneuver (δ_{sw} is the steering wheel angle). The dots correspond to the experimental results, the solid lines to the high-fidelity simulator (see Section IV), and the dash-dotted lines to the internal model.
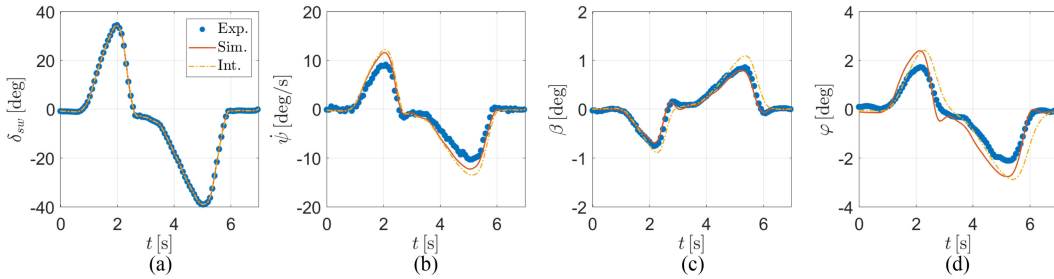
Fig. 4. Time profiles of steering wheel angle, yaw rate, sideslip angle, and roll angle during a transient steering maneuver at a vehicle speed of approx. 100 km/h. The dots correspond to the experimental results, the solid lines to the high-fidelity simulator (see Section IV), and the dash-dotted lines to the internal model.

$$J\left(x_0, u, p\right) = \int_0^{t_h} \|[\Delta T_{tot}\left(t\right), e_{\dot\psi}\left(t\right), P_{loss}\left(t\right), P_{brakes}\left(t\right),$$

$$\Delta T_{f,L}\left(t\right), \ \Delta T_{f,R}\left(t\right), \Delta f\left(t\right), z_{\sigma}\left(t\right), z_{\alpha_F}\left(t\right), z_{\alpha_R}\left(t\right)]^T\|_S^2 dt$$

$$+ w_f e_{\dot\psi}^2\left(t_h\right) \tag{36}$$

where $x_0 = x(0)$ is the initial value of the states of the system in (34), t_h is the prediction horizon, $S \in \mathbb{R}^{10\times10}$ is a strictly positive definite diagonal scaling matrix for weighting the elements of the stage cost, and w_f is the weight of the final cost relative to the equivalent yaw rate error, $e_{\dot\psi}$.

The contributions in (36) are based on

1) ΔT_{tot}, which aims to fulfill the torque request at the vehicle level, set by a higher level drivability and brake controller, and is defined as

$$\Delta T_{tot} = \sum_{j=1}^{4} T_j - T_{req} \tag{37}$$

where T_{req} is the total torque request, which is a function of the accelerator and brake pedal positions, and vehicle speed.

2) $e_{\dot\psi}$, which instigates the tracking of $\dot\psi_{ref}$:

$$e_{\dot\psi} = \dot\psi - \dot\psi_{ref} + w_i e_{int,\dot\psi} \tag{38}$$
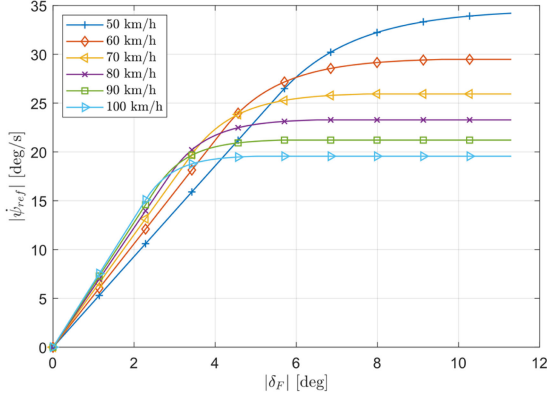
Fig. 5. Example of reference yaw rate curves as functions of the average front steering angle for different vehicle speeds and zero longitudinal acceleration.
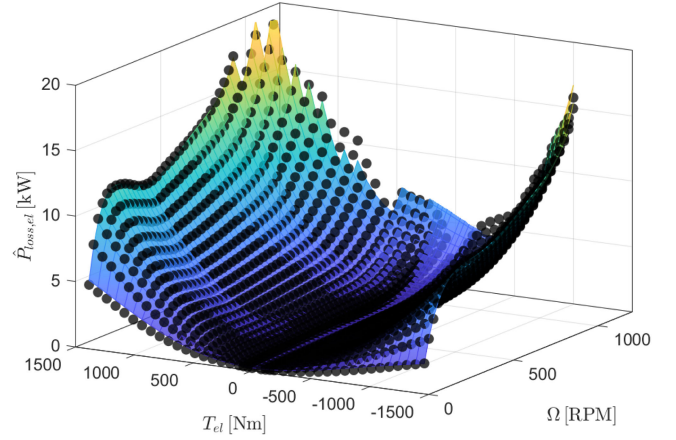

Fig. 6. Polynomial fitting of the measured powertrain power losses. The dots correspond to experimental data, whereas the mesh is the polynomial fitting.

where w_i is a coefficient that adjusts the integral contribution. In the controller implementation, $\dot{\psi}_{ref}$ is expressed through a map, as a function of steering angle, vehicle speed, and longitudinal acceleration, see an extract of the look-up table in Fig. 5, which targets a more agile behavior, i.e., with less understeer, than the vehicle without control, up to the limit handling condition, in which some conservativeness is imposed to enhance stability. Details on the generation method of the reference yaw rate map are reported in [1].

3) P_{loss}, which is the sum of the three main power loss contributions that are affected by the considered actuators

$$P_{loss}(t) = P_{loss,\sigma}(t) + P_{loss,\alpha}(t) + P_{loss,\,el}(t) \quad (39)$$

where

a) $P_{loss,\sigma}$ is the power loss due to the longitudinal tire slips, computed as the product of the longitudinal slip speed and longitudinal tire force [6], [19]:

$$P_{loss,\sigma}(t) = \sum_{j=1}^{4} -v_{x,slip,j}(t) F_{x,j}(t). \quad (40)$$

b) $P_{loss,\alpha}$ is the power loss due to the lateral tire slips, given by the product of the lateral slip speed and lateral tire force [6], [19]

$$P_{loss,\alpha}(t) = \sum_{j=1}^{4} -v_{y,slip,j}(t) F_{y,j}(t). \quad (41)$$

c) $P_{loss,el}$ are the power losses of the electric powertrains [6]

$$P_{loss,el}(t) = \sum_{j=1}^{4} \hat{P}_{loss,el}(T_{el,j}(t), \Omega_j(t)). \quad (42)$$

In (42), $\hat{P}_{loss,el}(t)$ is the power loss of each powertrain, expressed in the following polynomial form, function of the electric motor torque T_{el}, and motor speed Ω (which is the same

as the wheel speed in the considered direct drive IWMs)

$$\hat{P}_{loss,el}(T_{el}, \Omega) = \sum_{m=0}^{5} \left(\sum_{n=0}^{5} p_{m,n} T_{el}^n \right) \Omega^m \quad (43)$$

where the notation $p_{m,n}$ indicates the coefficients of the polynomial. The polynomial fitting that approximates the experimental powertrain power losses (data provided by the IWM supplier, Elaphe Propulsion Technologies), displayed in Fig. 6, is characterized by an R-squared value equal to 0.982.

As the implemented NMPC formulation outputs the front-to-total anti-roll moment distribution factor f, but does not affect the total anti-roll moment generated by the active suspension system, which is only a function of lateral acceleration according to (13), following conversations with the suspension system provider involved in the project, it was decided not to include the suspension actuation power losses in the cost function. In fact, in a first approximation, these power losses depend on the total anti-roll moment, rather than on f.

4) $P_{brakes}(t)$, which is the power dissipated in the friction brakes

$$P_{brakes}(t) = -\sum_{j=1}^{4} T_{bk,j}(t) \Omega_j(t). \quad (44)$$

Although this is a power loss, it is assigned a distinct weight with respect to $P_{loss}(t)$, to tune the intervention of the friction brakes.

5) $\Delta T_{f,L}$ and $\Delta T_{f,R}$, for tracking reference front-to-total motor torque distributions within each vehicle side

$$\Delta T_{f,L} = |[f_{T,L,opt} - 1] T_{el,1} + f_{T,L,opt} T_{el,3}| \quad (45)$$

$$\Delta T_{f,R} = |[f_{T,R,opt} - 1] T_{el,2} + f_{T,R,opt} T_{el,4}| \quad (46)$$

where $f_{T,L,opt}$ and $f_{T,R,opt}$ are the reference front-to-total motor torque distribution coefficients, which are computed offline for each combination of electric motor speed and total side torque demand, $T_{tot,side}$, to minimize the powertrain power losses. The online implementation approximates the solution calculated

offline through a hyperbolic tangent function, as described in [2] and [6]

$$f_{T,opt} = \zeta_2 + 0.5 \left[\zeta_3 - \zeta_2 \right] \tanh \left(\zeta_4 \left[T_{tot,side} - \zeta_1 \right] \right) \quad (47)$$

where the parameters ζ_1, ζ_2, ζ_3 and ζ_4 depend on the average motor speed on the considered side.

6) Δf, defined as:

$$\Delta f = |f - f_{pass}| \quad (48)$$

which smoothens the active suspension control action, and tends to keep the anti-roll moment distribution f in the neighborhood of its baseline value, f_{pass}, corresponding to the set-up for the passive vehicle.

7) The slack variables, z_σ, z_{α_F}, and z_{α_R}, which are used to set up the soft constraints.

B. Optimal Control Problem

The optimal control problem is formulated as

$$\min_u J\left(x_0, u, p\right)$$

$$\text{s.t.}$$

$i.$ $\dot{x}\,(t) = h\,(t, x\,(t)\,, u\,(t))\,,\, x\,(0) = x_0$

$ii.$ $T_{el,min,j} + T_{bk,min,j} \leq T_j\,(t) \leq T_{el,max,j}$

$iii.$ $T_1\,(t) + T_2\,(t) \leq \lambda \sum\limits_{j=1}^{4} T_j\,(t)$

$iv.$ $\sum\limits_{j=1}^{4} T_{el,j} \leq T_{tot,max}$

$v.$ $\sum\limits_{j=1}^{4} T_j \geq T_{tot,min}$

$vi.$ $f_{min} \leq f\,(t) \leq f_{max}$

$vii.$ $|M_{AR,Act,F}\,(t)| \leq M_{AR,Act,F,max}$

$viii.$ $|M_{AR,Act,R}\,(t)| \leq M_{AR,Act,R,max}$

$ix.$ $\sigma_{min} - z_\sigma\,(t) \leq \sigma_j\,(t) \leq \sigma_{max} + z_\sigma\,(t)$

$x.$ $\alpha_{F,min} - z_{\alpha_F}\,(t) \leq \alpha_j\,(t) \leq \alpha_{F,max} + z_{\alpha_F}\,(t)\,,\, j = 1,2$

$xi.$ $\alpha_{R,min} - z_{\alpha_R}\,(t) \leq \alpha_j\,(t) \leq \alpha_{R,max} + z_{\alpha_R}\,(t)\,,\, j = 3,4$

$xii.$ $z_\sigma\,(t) \geq 0$

$xiii.$ $z_{\alpha_F}\,(t) \geq 0$

$xiv.$ $z_{\alpha_R}\,(t) \geq 0 \quad (49)$

where u is the decision variable vector, consisting of the individual wheel torques, front-to-total anti-roll moment distribution factor, and slack variables, namely

$$u = [T_1, T_2, T_3, T_4, f, z_\sigma, z_{\alpha_F}, z_{\alpha_R}]^T. \quad (50)$$

The constraints ii-$vi)$ in (49) act on the torques; in particular, $ii)$ sets the upper and lower bounds for each wheel torque, where the subscripts "min" and "max" indicate the minimum and maximum values of the variable; $iii)$ imposes a front-to-total
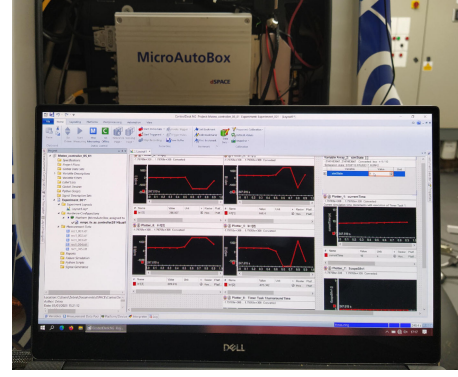

Fig. 7. Real-time implementation of the proposed controllers on a dSPACE MicroAutoBox unit.

braking torque distribution limitation at the wheels through the coefficient λ, output by the electronic brake distribution algorithm, which in production vehicles limits the rear wheel slip with respect to the front wheel slip in braking conditions, and is located externally to the NMPC, as an independent safety feature. This constraint is disabled in motoring conditions. $iv)$ and $v)$ set the upper ($T_{tot,max}$) and lower ($T_{tot,min}$) bounds for the total torques. $vi)$ limits the range of f; $vii)$ and $viii)$ limit the maximum absolute value of the anti-roll moment, calculated by a specific external function within the low-level controller of the suspension actuators; $ix)$–$xi)$ impose soft constraints on the slip ratios and slip angles; finally, xii–$xiv)$ impose the positive sign of the slack variables. The reduced number of slack variables with respect to the number of constraints limits the number of control variables, and thus the computational load.

The control problem formulation in (49) uses the following parameter vector, p, which includes the variables that are measured or estimated outside the NMPC, and are kept constant throughout the prediction horizon

$$p = [\delta_1, \ldots, \delta_4, a_{x,ext}, a_{y,ext}, \lambda, T_{el,min,1}, \ldots, T_{el,min,4},$$

$$T_{el,max,1}, \ldots, T_{el,max,4}, M_{AR,Act,F,max}, M_{AR,Act,R,max},$$

$$w_r, f_{min}, f_{max}]^T. \quad (51)$$

C. Controller Implementation

The NMPC algorithms were implemented via the ACADO toolkit [20], which offers a powerful interface for NMPC development, with the following settings: Gauss Newton Hessian approximation, multiple shooting discretization, fourth order implicit Runge Kutta integrator, and qpOASES solver. The controller sampling time was set to 35 ms, while the number of optimization steps was set to 2, which corresponds to a prediction horizon of 70 ms. The discretization time of the internal model is 1 ms, which ensures its numerical stability without significantly affecting the computational time. Extensive simulations showed that these parameterizations are a good compromise between performance and computational efficiency. The resulting controllers run in real-time on the dSPACE MicroAutoBox system (900 MHz, 16 Mb flash memory) in Fig. 7.
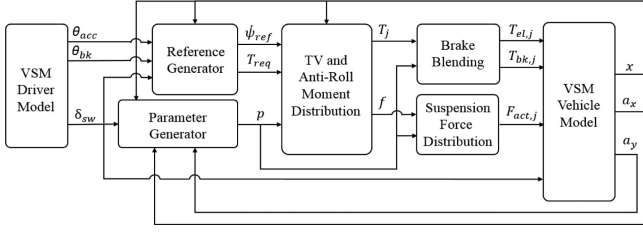
Fig. 8.   Simplified schematic of the simulation environment.

IV. SIMULATION RESULTS

A. Simulation Environment

The simulation environment (Fig. 8) consists of the following blocks.

1) The driver model, generating the accelerator and brake pedal positions, θ_{acc} and θ_{bk}, as well as the steering wheel angle δ_{sw}.

2) The reference generation block, defining T_{req} and $\dot{\psi}_{ref}$ starting from the driver inputs and measured or estimated signals, such as vehicle speed.

3) The electric powertrain and anti-roll moment distribution controller, generating T_j and f. In parallel with the proposed NMPC, a benchmarking controller was implemented, based on independent proportional integral (PI) contributions for the actuation of the direct yaw moment and front-to-total anti-roll moment distribution. The tuning of the direct yaw moment contribution ensures desirable tracking performance and stability, according to the design method in [21], while the PI controller computing the front-to-total anti-roll moment distribution was designed according to the model based method recently proposed in [10] and [11].

4) The brake blending controller, defining the torque distribution between IWMs and friction brakes, by prioritizing brake regeneration within each corner.

5) The suspension force allocator, generating the individual suspension actuator forces, $F_{act,j}$, which are given by

$$F_{act,j} = \frac{M_{AR,Act,i}}{b_i \, IR_i} \, (-1)^j \tag{52}$$

where IR_i, with $i = F, R$, is the installation ratio of the front/rear actuators.

6) The high-fidelity vehicle simulation model for control system assessment, implemented via the software package VSM by AVL [22], and parametrized with the data provided by the industrial partners of the EVC1000 project. Examples of experimental validation results in quasi-steady-state and transient conditions for the baseline configuration of the demonstrator vehicle are reported in Figs. 3 and 4.

7) The vehicle parameter generation block, which outputs p, as defined in (51).

B. Considered Configurations

The following vehicle control configurations are compared.

1) $f_{pass} + f_{T,pass}$, with active roll angle compensation through active suspension control with fixed front-to-total anti-roll moment distribution ratio $f_{pass} = 0.67$, which was selected to be aligned with the one of the vehicle configuration without active suspension actuators; zero direct yaw moment, i.e., the total wheel torque is the same on the left and right wheels; and front-to-total wheel torque distribution within each vehicle side according to the fixed ratio $f_{T,pass} = 0.5$, which is the natural baseline choice for a four-wheel-drive vehicle.

2) $f_{pass} + f_{T,act}$, with active roll angle compensation with fixed $f_{pass} = 0.67$; zero direct yaw moment; and variable front-to-total wheel torque distribution according to a ratio, $f_{T,act}$, defined in a look-up table function of the torque on the vehicle side and speed, to minimize the electric powertrain power loss. The $f_{T,act}$ map is the one used for deriving the approximate solution expressed by (47).

3) $f_{pass} + \text{TV}$ (NMPC) and $f_{pass} + \text{TV}$ (PI), including active roll angle compensation with fixed $f_{pass} = 0.67$, and TV control contributions based on the proposed NMPC or benchmarking PI. In $f_{pass} + \text{TV}$ (PI), the front-to-total wheel torque distribution within each vehicle side uses the fixed ratio $f_{T,pass} = 0.5$.

4) $f_{act} + \text{TV}$ (NMPC) and $f_{act} + \text{TV}$ (PI), including active roll angle compensation with active anti-roll moment distribution and TV, based on NMPC or PI control.

In summary, all considered arrangements use the active suspension actuators for roll moment compensation; 3) includes direct yaw moment control through TV, while 4) includes both direct yaw moment control through TV and anti-roll moment distribution control. Unless otherwise specified, the configurations in 3) and 4) track the reference yaw rate defined by the map in Fig. 5. In the remainder, the superscript "[1]" indicates controlled configurations using reference yaw rate maps aligned with the yaw rate response of the uncontrolled vehicle, i.e., $f_{pass} + f_{T,pass}$, while the superscript "[2]" indicates an NMPC calibration in which the weights on the power loss related terms (P_{loss}, P_{brakes}, $\Delta T_{f,L}$, $\Delta T_{f,R}$, z_σ, and z_{α_F}) of J are set to zero.

Despite the high number of weights, the tuning of the specific NMPC formulation is rather intuitive also for nonspecialists in model predictive control, as each cost function weight has a clear physical meaning. In the implementation phase, the yaw rate tracking weight of the NMPC cost function was set to achieve better tracking performance than with the benchmarking PI controllers. Then the weights of the power loss contributions of the NMPC cost function were designed to reduce the power losses.

Thanks to their limited computational burden, the $f_{pass} + f_{T,pass}$, $f_{pass} + f_{T,act}$, $f_{pass} + \text{TV}$ (PI) and $f_{act} + \text{TV}$ (PI) set-ups are implemented at 20 ms, i.e., at a lower step than the NMPC.

C. Ramp Steer Maneuver

The ramp steer maneuver consists of a steering wheel angle ramp applied at a rate of 1 deg/s, while the vehicle is kept at the constant speed of ∼100 km/h, for dry tarmac
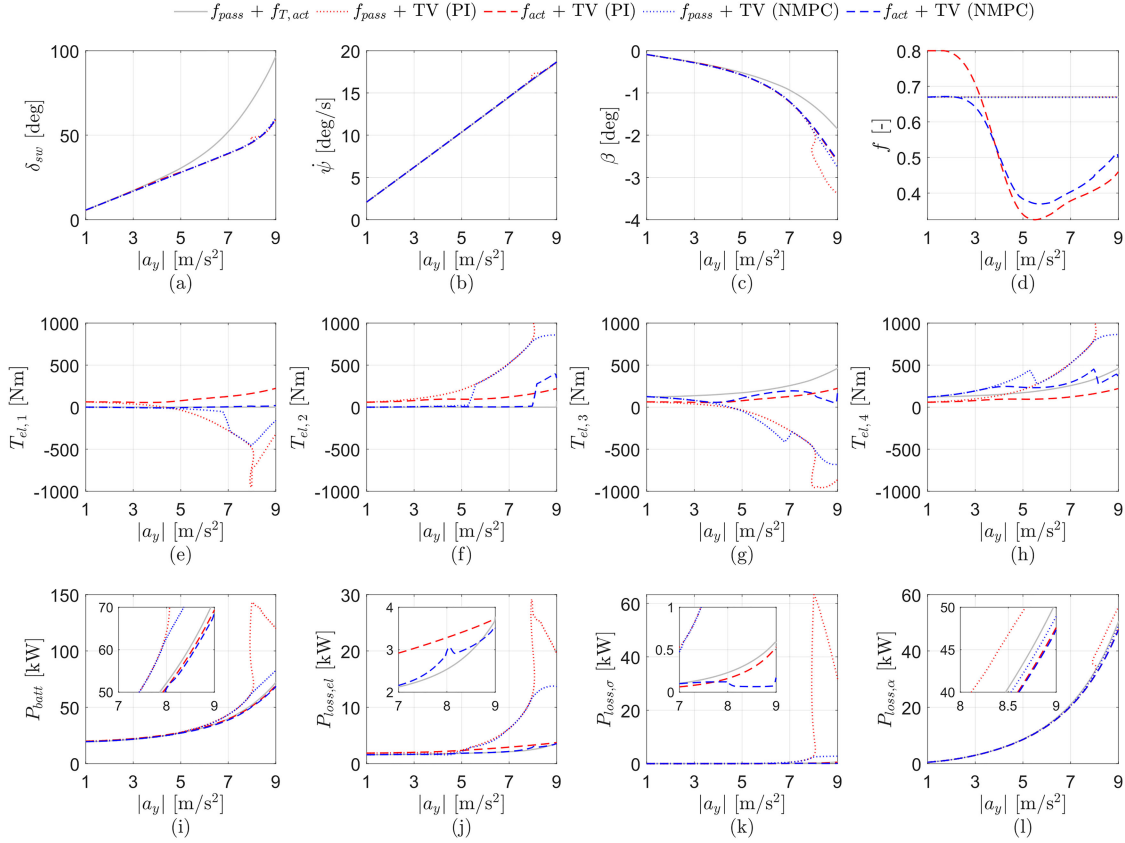
Fig. 9.   Summary plots for the ramp step steer maneuver.

TABLE II
PERFORMANCE INDICATORS FOR THE CONSIDERED VEHICLE CONFIGURATIONS DURING THE RAMP STEER MANEUVER

	$\overline{D}_{M_z}$ [Nm]	$\overline{D}_f$ [-]	$\overline{P}_{loss+bk}$ [kW]		
a_y [m/s^2]	1-9	1-9	1-3	3-6	6-9
$f_{pass} + f_{T,pass}$	0	0.00	3.43	9.58	31.52
$f_{pass} + f_{T,act}$	0	0.00	3.13	9.10	30.79
$f_{pass} + $ TV (NMPC)	899	0.00	3.13	9.36	37.68
$f_{act} + $ TV (NMPC)	170	0.17	3.13	8.99	29.42
$f_{pass} + $ TV (PI)	1051	0.00	3.41	9.57	57.13
$f_{act} + $ TV (PI)	23	0.22	3.43	9.47	30.12
$f_{pass} + $ TV (NMPC)[1]	24	0.00	3.14	9.12	30.88
$f_{act} + $ TV (NMPC)[1]	64	0.01	3.14	9.12	30.66
$f_{pass} + $ TV (PI)[1]	30	0.00	3.43	9.58	31.42
$f_{act} + $ TV (PI)[1]	9	0.07	3.43	9.63	31.46
$f_{act} + $ TV (NMPC)[2]	87	0.17	3.23	9.31	29.76

conditions. The main variables are plotted in Fig. 9, while Table II includes a selection of performance indicators as follows.

1) $\bar{D}_{M_z}$, i.e., the average value of $|T_2 + T_4 - T_1 - T_3|$ for all the operating points in the 1–9 m/s^2 lateral acceleration (a_y) range. This index measures the intensity of the direct yaw moment control effort.

2) $\bar{D}_f$, i.e., the anti-roll moment distribution index, calculated as the average value of $|f - f_{pass}|$ in the 1–9 m/s^2 lateral

acceleration range, which measures the intensity of the active suspension control effort toward yaw rate tracking.

3) $\bar{P}_{loss+bk}$, i.e., the average value of $P_{loss} + P_{brakes}$, computed from the data within three lateral acceleration ranges, namely 1–3 m/s^2, 3–6 m/s^2, and 6–9 m/s^2.

Given the absence of direct yaw moment and anti-roll moment distribution actuation and the relatively low traction force, the cornering response of the rule based cases $f_{pass} + f_{T,pass}$ and $f_{pass} + f_{T,act}$ is mainly determined by the vehicle hardware set-up, e.g., in terms of tires, mass distribution and suspensions, rather than by the controller. The look-up table based side torque distribution of $f_{pass} + f_{T,act}$ effectively reduces P_{loss} throughout the lateral acceleration domain. In general, in the low a_y region, where the tire slip power losses are negligible, the power loss results are substantially aligned, and ∼9% lower than in $f_{pass} + f_{T,pass}$, for all controllers considering the optimal side torque distribution based on the powertrain power loss, either as a look-up table or through (47). The $f_{pass} + $ TV and $f_{act} + $ TV configurations track the reference understeer characteristic defined by the yaw rate map in Fig. 5, which brings a significant extension of the linear vehicle response region up to a lateral acceleration of ∼7.5 m/s^2, against the ∼5 m/s^2 of $f_{pass} + f_{T,pass}$ and $f_{pass} + f_{T,act}$ [Fig. 9(a)]. Consistently with the reduced level of understeer and more reactive steady-state cornering behavior, the TV cases show marginally higher sideslip angle values [Fig. 9(c)] than the configurations without direct yaw moment control.

Despite the substantial coincidence of their cornering responses, $f_{pass} + $ TV (NMPC) and $f_{act} + $ TV (NMPC) impose very different control actions. In fact, in presence of f_{act}, for a wide range of a_y it is more energy-efficient to achieve the reference understeer characteristic by reducing f [Fig. 9(d)], which lowers the magnitude of the direct yaw moment (see the $\bar{D}_{M_z}$ values) and IWM torques [Fig. 9(e)–(h)]. Hence, for $f_{act} + $ TV all IWMs are always in traction, whilst for $f_{pass} + $ TV the IWMs on the inner side of the corner operates in regeneration for $a_y > \sim 5$ m/s².

On the one hand, the consequence is that at high a_y the selected sport-oriented reference understeer characteristic, although desirable from the viewpoint of the vehicle cornering response, increases the power loss of the $f_{pass} + $ TV set-ups, which have the highest $\bar{P}_{loss+bk}$ among all configurations for 6 m/s² $< a_y <$ 9 m/s², see [4] and [6] for the analysis of the effect of the understeer characteristic on the power consumption of TV controlled vehicles. On the other hand, starting from ~ 4 m/s², when the lateral load transfer becomes significant, the active anti-roll moment distribution of $f_{act} + $ TV (NMPC) offers remarkable power consumption reductions [see the battery power P_{batt} profiles in Fig. 9(i)] with respect to the $f_{pass} + $ TV configurations, because of the lower powertrain and longitudinal tire slip power losses [Fig. 9(j) and (k)]. As expected, since the understeer and sideslip characteristics are the same, the lateral tire slip power losses [Fig. 9(l)] are substantially coincident for all $f_{pass} + $ TV and $f_{act} + $ TV configurations.

The effectiveness of the proposed NMPC implementations is highlighted by the comparison with the corresponding PI configurations. In the $f_{pass} + $ TV case, the power loss reduction achieved by the NMPC is $> 2\%$ for 1 m/s² $< a_y <$ 6 m/s², and becomes substantial for $a_y > 6$ m/s², especially because of the NMPC capability of limiting longitudinal tire slip, which compromises the sideslip angle characteristics of $f_{pass} + $ TV (PI) for $a_y > 8$ m/s². Conversely, the $f_{act} + $ TV (PI) configuration smoothly follows the desired understeer characteristic, although with consistently higher $\bar{P}_{loss+bk}$ values than those of $f_{act} + $ TV (NMPC). The profile of f for the $f_{act} + $ TV (PI) configuration starts from a different value from the one of the corresponding NMPC, because of the effect of the PI control action in the initial part of the test (not reported in the graph). Table II also includes the results for $f_{pass} + $ TV[1] and $f_{act} + $ TV[1]. With this reference yaw rate setting, also the NMPC configuration based on TV control reduces $\bar{P}_{loss+bk}$ with respect to the $f_{pass} + f_{T,pass}$ case, e.g., from 31.52 to 30.88 kW in the 6–9 m/s² range, while the inclusion of the anti-roll moment distribution brings further improvements, e.g., $\bar{P}_{loss+bk}$ in the 6–9 m/s² interval amounts to 29.76 kW. Also in this case, the $\bar{P}_{loss+bk}$ results consistently favor the NMPC with respect to the PI, with average 5% power loss reductions across the lateral acceleration range for $f_{pass} + $ TV[1] and $f_{act} + $ TV[1]. Interestingly, because of the lack of integration between TV and anti-roll moment distribution and the impossibility to formally consider the energy efficiency aspects in the control design, in the PI configuration $f_{act} + $ TV[1] consumes more than $f_{pass} + $ TV[1]. The $f_{act} + $ TV (NMPC)[2] configuration, which excludes the power loss reduction terms from the cost function and tracks

the yaw rate in Fig. 5, brings a power loss increase ranging from 1% to 4% with respect to $f_{act} + $ TV (NMPC), which confirms the effectiveness of the proposed energy-efficient formulations.

In summary, the important conclusion of the ramp steer analysis is that for medium-to-high lateral accelerations the redundant actuation of the $f_{act} + $ TV configuration not only permits enhanced flexibility in shaping the vehicle cornering response, but also achieves an evident and consistent power loss reduction with respect to all other cases, as it allows the powertrains and tires to work in their most efficient region, independently from the selected reference understeer characteristic.

D. Multiple Step Steer Maneuver

The considered multiple step steer is an extreme transient test, and consists of a rapid sequence of fast steering wheel inputs with a magnitude of ~ 110 deg, applied at a rate > 500 deg/s, see Fig. 10(a), while maintaining a constant 20% accelerator pedal position, from an initial speed of ~ 107 km/h, with a tire-road friction factor corresponding to dry tarmac conditions.

The profiles of the main variables are in Figs. 10 and 11, while Table III reports the relevant performance indicators, which, in addition to those in Table II, include

1) $\Delta \dot{\psi}_{RMS}$, i.e., the root mean square (RMS) value of the yaw rate error, which evaluates the tracking performance of the controller and overall vehicle agility.

2) $|\beta_{max}|$, i.e., the maximum absolute value of the vehicle body sideslip angle, which is a vehicle stability indicator.

3) $\Delta F_{z,RMS}^y$, i.e., the RMS value of $F_{z,1} + F_{z,3} - F_{z,2} - F_{z,4}$, which assesses the magnitude of the total lateral load transfer, and thus vehicle rollover propensity.

4) $\bar{D}_{cut}$, i.e., the average value of $D_{cut} = T_{req} - (T_1 + T_2 + T_3 + T_4)$, which expresses the magnitude of the total wheel torque reduction with respect to the driver torque request, e.g., to facilitate yaw rate tracking or meet tire slip constraints.

5) V_{end}, i.e., the vehicle speed at the end of the test, which assesses the total power loss at the vehicle level, as the maneuver is executed at constant accelerator pedal position.

Differently from the ramp steer maneuver, the performance indicators for the multiple step steer are computed across the whole lateral acceleration range. The results show the following.

1) The NMPC configurations ensure stable yaw rate tracking [Figs. 10(b) and 11], with very small overshoots following each steering angle variation, and effectively constrain sideslip angle [Fig. 10(c)], with $|\beta_{max}|$ values lower than 2.5 deg for the formulations considering all cost function terms, while the exclusion of the power loss terms of J yields higher $|\beta_{max}|$. On the contrary, $f_{pass} + f_{T,pass}$ and $f_{pass} + f_{T,act}$ reach $|\beta_{max}|$ values in excess of 14 deg, and experience significant delays with respect to the steering angle profile in returning to the condition of zero yaw rate and sideslip angle at the end of the test. Although the PI controllers provide desirable vehicle response, the NMPC configurations achieve better yaw rate tracking performance than the corresponding PI counterparts, as demonstrated by the $\Delta \dot{\psi}_{RMS}$ values in Table III, and the yaw rate profiles in Fig. 11.

2) The front-to-total anti-roll moment distribution profile of $f_{act} + $ TV [Fig. 10(e)] shows pronounced peaks in the transients
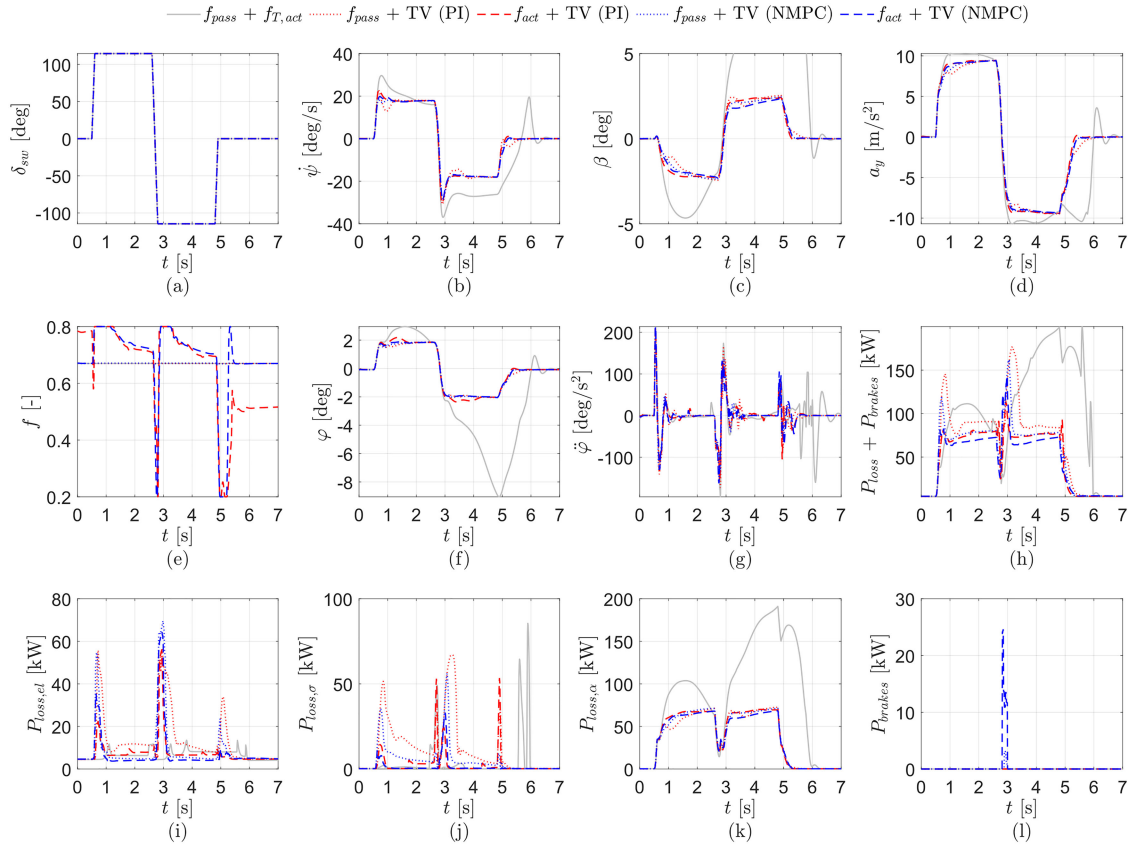
Fig. 10. Summary plots for the multiple step steer maneuver.

TABLE III
PERFORMANCE INDICATORS FOR THE CONSIDERED VEHICLE CONFIGURATIONS DURING THE MULTIPLE STEP STEER MANEUVER

|	$\Delta\dot\psi_{RMS}$ [deg/s]	$|\beta_{max}|$ [deg]	$\Delta F_{z,RMS}^{y}$ [kN]	$\overline{D}_{M_z}$ [Nm]	$\overline{D}_{cut}$ [Nm]	$\overline{D}_f$ [-]	V_{end} [km/h]	$\overline{P}_{loss+bk}$ [kW]
$f_{pass} + f_{T,pass}$	-	14.66	21.83	247	245	0.00	92.2	96.13
$f_{pass} + f_{T,act}$	-	14.74	21.84	246	244	0.00	92.1	96.59
$f_{pass} + $ TV (NMPC)	2.68	2.49	16.52	768	179	0.00	115.6	52.87
$f_{act} + $ TV (NMPC)	2.66	2.37	16.54	619	215	0.08	115.1	46.31
$f_{pass} + $ TV (PI)	3.62	2.58	16.38	925	154	0.00	115.4	62.60
$f_{act} + $ TV (PI)	3.39	2.43	16.87	489	162	0.12	114.7	49.11
$f_{act} + $ TV (NMPC)[2]	2.67	2.96	16.66	850	156	0.10	116.1	53.61
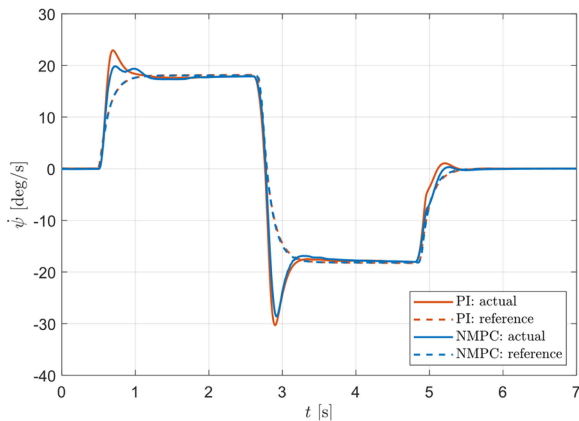
Fig. 11. Reference and actual yaw rate profiles for $f_{act} + $ TV (PI) and $f_{act} + $ TV (NMPC).

following each steering input, which contribute to the reduction of the yaw rate oscillations. This behavior can be considered realistic and implementable, as it is similar to the one observed in the suspension control analysis in [10], including experimental vehicle validation. On average, the anti-roll moment distribution contribution is biased towards the front axle, and tends to increase the level of understeer and vehicle stabilization. The PI and NMPC configurations produce similar f profiles, with the exclusion of the initial and final parts of the test, which are not meaningful because a_y is approximately zero [Fig. 10(d)].

3) The NMPC and PI configurations bring a reduction of the lateral load transfers during the steering transients, highlighted by the lower values of $\Delta F_{z,RMS}^{y}$. With respect to $f_{act} + $ TV, the increase of $\Delta F_{z,RMS}^{y}$ is negligible for $f_{pass} + $ TV, but it exceeds 20% for $f_{pass} + f_{T,pass}$ and $f_{pass} + f_{T,act}$. After the second steering wheel stroke and the sign inversion of

the steering angle, both the front and rear internal wheels lift from the ground in $f_{pass} + f_{T,pass}$ and $f_{pass} + f_{T,act}$, posing a rollover risk, whilst in the NMPC and PI configurations wheel lift only occurs on the front inner corners for more limited time. Wheel lift, together with the subsequent wheel spinning and individual speed-dependent motor torque saturations, is the cause for the marginal non-zero values of $\bar{D}_{M_z}$ and $\bar{D}_{cut}$ also in the configurations without TV.

4) The NMPC set-ups bring very major power loss reductions in transient conditions, with $\bar{P}_{loss+bk}$ values below 54 kW, with respect to the $\sim$96 kW of $f_{pass} + f_{T,pass}$ and $f_{pass} + f_{T,act}$. This difference is mainly caused by the reduction of the lateral tire slip power losses, and is confirmed by the values of V_{end}, ranging from 92.1 km/h for $f_{pass} + f_{T,act}$, to 116.1 km/h for $f_{act} + \text{TV (NMPC)}^2$. Such final vehicle speed increment is achieved despite the torque request reductions, measured by $\bar{D}_{cut}$, imposed by the NMPC implementations in the critical phases of the test, immediately after the δ_{sw} variations, to facilitate reference yaw rate tracking. The torque reductions also imply moderate friction brake actuation in very limited parts of the maneuver. Also in this respect, the NMPC solution with active front-to-total anti-roll moment distribution outperforms the one based on TV only, with $>12\%$ $\bar{P}_{loss+bk}$ reduction. Significant advantages in terms of energy-efficiency are provided by the NMPC set-ups with respect to the corresponding PI alternatives, with 16% and 6% $\bar{P}_{loss+bk}$ reductions for the $f_{pass} + \text{TV}$ and $f_{act} + \text{TV}$ configurations. Finally, the inclusion of the power loss terms in the NMPC formulation brings a $>13\%$ $\bar{P}_{loss+bk}$ decrease, see the results for $f_{act} + \text{TV (NMPC)}$ and $f_{act} + \text{TV}$ $(\text{NMPC})^2$.

V. CONCLUSION

The article presented a novel NMPC implementation for TV and front-to-total anti-roll moment distribution control, considering vehicle dynamics as well as powertrain and tire slip power loss aspects in its cost function. The integrated controller was compared with its simplified version including TV only, its simplified version excluding the power loss aspects, two PI implementations for the same actuators, and two rule based algorithms. The simulation results for an electric vehicle with IWMs, active suspension actuators and a brake-by-wire system show the following.

1) In quasi-steady-state cornering, the integration of active suspension and TV for vehicle dynamics control provides a consistent power loss reduction across the whole range of lateral accelerations, rather independently from the selected reference understeer characteristic, which is a major benefit of the active suspension system. In fact, for medium-to-high lateral accelerations, the variable front-to-total anti-roll moment distribution is actuated by the proposed NMPC to make the electric powertrains and tires work in their most effective conditions.

2) Although TV on its own offers significant shaping capability of the understeer characteristic, its power loss performance is strongly affected by the selected reference yaw rate response, which, for the specific vehicle parameters, results in a trade-off between desirable vehicle cornering behavior and energy efficiency.

3) In quasi-steady-state cornering, an appropriate selection of the front-to-total wheel torque distribution within each vehicle side can make rule based algorithms very effective in terms of power consumption performance, especially at low-to-medium lateral accelerations.

4) In extreme transient conditions, the advantages of advanced nonlinear control are evident in terms of yaw rate and sideslip damping, limitation of the total lateral load transfer, total power loss reduction, as well as increase of the exit speed, with a systematic benefit in all aspects brought by the integrated TV and active suspension solution.

5) The proposed NMPC consistently outperforms the corresponding benchmarking PI configurations, and its own version excluding consideration of the power loss aspects.

Future developments will include the assessment of the integrated controller in a wider range of conditions, and its experimental evaluation on an electric vehicle demonstrator.

REFERENCES

[1] L. De Novellis *et al.*, "Direct yaw moment control actuated through electric drivetrains and friction brakes: Theoretical design and experimental assessment," *Mechatronics*, vol. 26, pp. 1–15, 2015.

[2] A. Pennycott, L. De Novellis, A. Sabbatini, P. Gruber, and A. Sorniotti, "Reducing the motor power losses of a four-wheel drive, fully electric vehicle via wheel torque allocation," *Proc. Inst. Mech. Engineers, D, J. Automobile Eng.*, vol. 228, no. 7, pp. 830–839, 2014.

[3] X. Hu, P. Wang, Y. Hu, and H. Chen, "A stability-guaranteed and energy-conserving torque distribution strategy for electric vehicles under extreme conditions," *Appl. Energy*, vol. 259, 2020, Art. no. 114162.

[4] G. De Filippis, B. Lenzo, A. Sorniotti, P. Gruber, and W. D. Nijs, "Energy-efficient torque-vectoring control of electric vehicles with multiple drivetrains," *IEEE Trans. Veh. Technol.*, vol. 67, no. 6, pp. 4702–4715, Jun. 2018.

[5] S. Koehler, A. Viehl, O. Bringmann, and W. Rosenstiel, "Energy-efficiency optimization of torque vectoring control for battery electric vehicles," *IEEE Intell. Transp. Syst. Mag.*, vol. 9, no. 3, pp. 59–74, Jul. 2017.

[6] A. Parra, D. Tavernini, P. Gruber, A. Sorniotti, A. Zubizarreta, and J. Pérez, "On nonlinear model predictive control for energy-efficient torque-vectoring," *IEEE Trans. Veh. Technol.*, vol. 70, no. 1, pp. 173–188, Jan. 2021.

[7] K. Shimada and Y. Shibahata, "Comparison of three active chassis control methods for stabilizing yaw moments," SAE Tech. Paper 940870, 1994.

[8] D. E. Williams and W. M. Haddad, "Nonlinear control of roll moment distribution to influence vehicle yaw characteristics," *IEEE Trans. Control Syst. Technol.*, vol. 3, no. 1, pp. 110–116, Mar. 1995.

[9] A. Sorniotti and N. D'Alfio, "Vehicle dynamics simulation to develop an active roll control system," SAE Tech. Paper 2007-01-0828, 2007.

[10] M. Ricco *et al.*, "On the design of yaw rate control via variable front-to-total anti-roll moment distribution," *IEEE Trans. Veh. Technol.*, vol. 69, no. 2, pp. 1388–1403, Feb. 2020.

[11] M. Ricco *et al.*, "On the model-based design of front-to-total anti-roll moment distribution controllers for yaw rate tracking," *Veh. Syst. Dyn.*, pp. 1–28, 2020.

[12] G. Long, F. Ding, N. Zhang, J. Zhang, and A. Qin, "Regenerative active suspension system with residual energy for in-wheel motor driven electric vehicle," *Appl. Energy*, vol. 260, 2020, Art. no. 114180.

[13] A. H. Ahangarnejad, S. Melzi, and M. Ahmadian, "Integrated vehicle dynamics system through coordinating active aerodynamics control, active rear steering, torque vectoring and hydraulically interconnected suspension," *Int. J. Automot. Technol.*, vol. 20, no. 5, pp. 903–915, 2019.

[14] J. Gerhard *et al.*, "Robust yaw control design with active differential and active roll control systems," *IFAC Proc. Volumes*, vol. 38, no. 1, pp. 73–78, 2005.

[15] H. Her, K. Yi, J. Suh, and C. Kim, "Development of integrated control of electronic stability control, continuous damping control and active anti-roll bar for vehicle yaw stability," *IFAC Proc. Vol.*, vol. 46, no. 21, pp. 83–88, 2013.

[16] H. Her, Y. Koh, E. Joa, K. Yi, and K. Kim, "An integrated control of differential braking, front/rear traction, and active roll moment for limit handling performance," *IEEE Trans. Veh. Technol.*, vol. 65, no. 6, pp. 4288–4300, Jun. 2016.

[17] E. Armengaud *et al.*, "EVC1000–integrated corner solution for innovative electric vehicles," in *Proc. 8th Transp. Res. Arena (TRA)*, Helsinki, Finland, 2020.

[18] L. Grüne and J. Pannek, "Nonlinear model predictive control," Springer, 2011.

[19] T. Kobayashi, E. Katsuyama, H. Sugiura, Y. Hattori, E. Ono, and M. Yamamoto, "Theoretical analysis of tyre slip power dissipation mechanism using brush model," *Veh. System Dyn.*, vol. 58, no. 8, pp. 1242–1256, 2020.

[20] B. Houska, H. J. Ferreau, and M. Diehl, "ACADO toolkit–an open source framework for automatic control and dynamic optimization," *Optimal Control Appl. Methods*, vol. 32, no. 3, pp. 298–312, 2011.

[21] Q. Lu, A. Sorniotti, P. Gruber, J. Theunissen, and J. De Smet, "H_∞ loop shaping for the torque-vectoring control of electric vehicles: Theoretical design and experimental assessment," *Mechatronics*, vol. 35, pp. 32–43, 2016.

[22] Accessed: 20 Sep. 2020. [Online]. Available: https://www.avl.com/documents/10138/2095827/AVL+VSM+4%E2%84%A2+-+Solution+Brochure

Matteo Dalboni received the M.Sc. degree in mechanical engineering and the Ph.D. degree in information technology from the University of Parma, Parma, Italy, in 2017 and 2021, respectively.

His research interests include vehicle dynamics and control, with focus on torque allocation in fully electric vehicles with independent drives and multiple actuations.

Davide Tavernini received the M.Sc. degree in mechanical engineering and the Ph.D. degree in dynamics and design of mechanical systems from the University of Padova, Padua, Italy, in 2010 and 2014, respectively.

He is currently a Lecturer of advanced vehicle engineering with the University of Surrey, Guildford, U.K. His research interests include vehicle dynamics modeling and control applied to electric and hybrid electric vehicles.

Umberto Montanaro received the M.Sc. degree in computer science engineering and the Ph.D. degrees in control engineering and mechanical engineering from the University of Naples Federico II, Naples, Italy, in 2005, 2009, and 2016, respectively.

He is currently a Lecturer of control engineering and autonomous systems with the University of Surrey, Guildford, U.K. His research interests include adaptive control, and control of piecewise-affine, mechatronic, and automotive systems.

Alessandro Soldati (Member, IEEE) received the B.Sc. and M.Sc. degrees in electronic engineering in 2011 and 2013, respectively, from the University of Parma, Parma, Italy.

He is currently a Researcher of Power Electronics and Energy Engineering with the University of Parma, Parma, Italy. In 2017, he cofounded the spin-off company eDriveLAB, Parma, Italy in the field of vehicle electrification, where he is currently the Chief Technical Officer.

Carlo Concari (Member, IEEE) received the Ph.D. degree in information technology from the University of Parma, Parma, Italy, in 2006.

He is currently an Associate Professor with the Department of Engineering and Architecture, University of Parma. His research interests include power electronics, drive control, electric propulsion, static power converters, and electric machines diagnostics.

Miguel Dhaens received the M.Sc. degree in electro-mechanical engineering from KIH, Ostend, Belgium.

He is currently an Engineering Manager with the Global Research Ride Performance Team, Tenneco, Limburg, Belgium, and responsible for defining the research road map and coordinating the global research activities of Tenneco's Ride Performance business.

Aldo Sorniotti (Member, IEEE) received the M.Sc. degree in mechanical engineering and the Ph.D. degree in applied mechanics from the Politecnico di Torino, Turin, Italy, in 2001 and 2005, respectively.

He is currently a Professor of advanced vehicle engineering with the University of Surrey, Guildford, U.K. His research interests include vehicle dynamics control and transmission systems for electric and hybrid electric vehicles.